Gadolinium-loaded LTL nanosized zeolite for efficient oxygen delivery and magnetic resonance imaging

Abdallah Amedlous, C Hélaine, Rémy Guillet-Nicolas, Oleg Lebedev, Valable Samuel, Svetlana Mintova

To cite this version:

Abdallah Amedlous, C Hélaine, Rémy Guillet-Nicolas, Oleg Lebedev, Valable Samuel, et al.. Gadolinium-loaded LTL nanosized zeolite for efficient oxygen delivery and magnetic resonance imaging. Inorganic Chemistry Frontiers, 2023, 10 (9), pp.2665-2676. 10.1039/D3QI00169E . hal-04250335

HAL Id: hal-04250335

https://normandie-univ.hal.science/hal-04250335v1

Submitted on 19 Oct 2023

Gadolinium-loaded LTL nanosized zeolite for efficient oxygen delivery and magnetic resonance imaging

Abdallah Amedlous[a], Charly Hélaine[b], Rémy Guillet-Nicolas[a], Oleg Lebedev[c], Samuel Valable*[b], Svetlana Mintova*[a]

[a] Normandie Université, ENSICAEN, CNRS, Laboratoire Catalyse et Spectrochimie (LCS), 14050 Caen, France.
[b] Normandie Université, UNICAEN, CNRS, ISTCT, GIP CYCERON, 14000 Caen, France
[c] Normandie Université, ENSICAEN, UNICAEN, CNRS, Laboratoire de Cristallographie et Science des Matériaux (CRISMAT), 14050 Caen, France.

*E-mails: svetlana.mintova@ensicaen.fr; valable@cyceron.fr

Abstract

The key challenges in finding efficient gas carriers for biomedical applications are related to the kinetics of gas adsorption/desorption of nontoxic materials over an appropriate time intervals, specifically targeting the affected area. Herein, we report the preparation of nanosized gadolinium (Gd-LTL) zeolite crystals with a diameter of 10−15 nm for oxygen delivery combined with magnetic resonance imaging (MRI) study. The partial ion-exchange of potassium (K) extra framework cations used for the synthesis of nanosized K-LTL zeolite with paramagnetic gadolinium (Gd, 1.53 wt%) changed considerably its adsorption capacity for O_2. The nanosized Gd-LTL zeolite retained high colloidal stability, remarkable crystallinity and no leaching of Gd ions was observed. In addition, the *in vitro* toxicity study performed in human glioblastoma-derived cell lines revealed that nanosized K-LTL and Gd-LTL nanosized zeolites showed no toxicity even at high concentrations. This study provides promising guidelines regarding the design of smart biocompatible nanosized zeolites coupling gas-delivery and MRI proprieties.

Keywords: zeolite LTL, injectable nanoparticles, biocompatibility, oxygen delivery, biomedical application

Introduction

Zeolites are microporous, crystalline materials with well-defined compositions and structures with regular pores and cavities of molecular dimensions [1,2]. Zeolite synthesis remains an active field of research and finding new nontraditional applications are highly desired including in biomedicine. The application of zeolites is driven by their physicochemical properties, i.e., chemical composition, pore size, crystalline structure, shape/size of particles as well as chemical/thermal and colloidal stability [3–6]. Currently, there are 255 types zeolite frameworks according to the International Zeolite Association (IZA) database, and most of them are used for catalysis, gas adsorption, and separation [7]. In spite of this versatility, several zeolites have been considered for biomedical applications [8]. In recent years, considerable efforts have been devoted to the decrease of zeolite crystal size from micron to nanoscale dimensions resulting in nanozeolites with large surface area, high stability in suspension, short diffusion length, and accessible active sites [9–12]. In addition, the synthesis of nanosized zeolites in the absence of organic templates is highly desired for applications in the biomedical field. The presence of organic template in zeolites required activation at elevated temperatures resulting in irreversible agglomeration and not stabilization of injectable colloidal suspensions [13–15]. While the organic template-free hydrothermal synthesis allowed the preparation of biocompatible zeolites. The feasibility of using nanosized zeolites for biomedical applications has been demonstrated from several groups already[12,16]. For instance, the CO_2 and O_2 sorption properties of faujasite (Na-FAU-X) was controlled by partial ion-exchange of the sodium extra-framework cations by trivalent metals (Gd^{3+}, Ce^{3+}) [17]. The high suspension stability and non-toxicity of nanosized FAU zeolite showed advantages as hyperoxic/hypercapnic gas carriers for glioblastoma treatment[18]. More recently, nanosized FAU zeolite with luminescent properties was developed enabling to track the fate of zeolites *in vitro* experiments on cell culture[19]. Additionally, several studies have examined the efficiency of nanozeolites such as FAU, LTA, and LTL as drug carriers, therapeutic agents, and probes for magnetic resonance imaging[20–23]. Nevertheless, relatively few studies have explored the use of nanosized zeolites as oxygen delivery systems for hypoxic tumor reoxygenation. Oxygen supply in tumors is highly desired, even transiently because a lack of oxygen is associated with tumor development and resistance to treatment[24,25]. The key challenge of the oxygen delivery system is to release the oxygen molecules over an appropriate time period and specifically target the affected area. Therefore, the development of novel safer nanomaterials with controllable oxygen- release feature for targeted gas therapy applications is urgently needed.

Zeolite LTL is an interesting candidate for this purpose since it is composed of uniform one-dimensional 12-MR rings running along the c-axis [001] of the crystals with a pore diameter of 0.71 x 0.71 nm, being suitable to host many gas molecules of interest. The LTL zeolite is hexagonal with a space group P6/mmm. The LTL structure is characterized by cancrinite cages linked by double 6-rings (D6R) leading to the formation of columns along the c axis resulting in 12-membered rings (12MR). The classical synthesis of LTL zeolites is performed in potassium-rich aluminosilicate precursors; by varying the amount of potassium cations, the state of the precursor can be varied from dense to clear suspensions. In the LTL zeolite, three extra-framework K^+ cations sites are present: in the center of the cancrinite cage (site K_1), in the center of the 8MR channel midway between adjacent cancrinite cages (site K_2), and near the walls of the main 12MR channel (site K_3)[26,27]. Cations-exchange in aqueous dispersions of zeolite-LTL always occurs in the K_3 sites, while the K_2 ones are only involved when K^+ is substituted by cations with similar ionic sizes, e.g. NH_4^+[23,28,29], and the K_1 sites are not accessible for exchange. In addition, the ion-exchange process can also generate new cation sites depending on the substituted ions[28].

In this work, we describe the synthesis of organic template-free nanosized zeolite L (LTL) using only K^+ as an inorganic structure-directing agent. Loading of Gd^{3+} in LTL zeolite was achieved *via* an ion-exchange procedure. Gd^{3+} was selected as a positive contrast agent in order to improve the clarity and definition of the tumor using MRI. The as-prepared K-LTL nanosized zeolite crystals exhibit high colloidal stability and homogenous particle sizes with dimensions of 10−15 nm and Si/Al ratio of 2.59. In addition, *in vitro* toxicity experiments were performed in human glioblastoma-derived cell lines, and the results confirm that nanocrystals are safe and non-toxic. Furthermore, the O_2 adsorption capacity of the LTL samples was investigated by adsorption isotherms and i*n situ* Fourier transform infrared (FTIR) spectroscopy. The high oxygen release in hypoxic conditions and the T1 relaxivity of the Gd-LTL nanocrystals with great potential for MRI are demonstrated.

Experimental section

1.1 Chemicals

Potassium hydroxide (KOH, 90 %), sodium hydroxide pellets (NaOH, 98%), colloidal silica (SiO_2, Ludox SM30, 30%), and gadolinium nitrate hexahydrate ($Gd(NO_3)\cdot 6H_2O$, 99.99%) were purchased from Sigma-Aldrich. Aluminum hydroxide ($Al(OH)_3$, 76.5%) was purchased from Alfa Aesar. All reagents were used as received without further purification. Mili-Q water was used for all synthesis and purification of samples.

1.2 Synthesis of LTL nanocrystals

The initial chemical composition used for the synthesis of nanosized LTL zeolite was 5 K_2O: 10 SiO_2: 0.5 Al_2O_3: 200 H_2O. Typically, in 8 g water, aluminum hydroxide (2.1 g) and potassium hydroxide (0.51 g) were dissolved and stirred until the mixture became transparent. The silica solution was prepared by mixing 10 g of Ludox® SM and potassium hydroxide (1.0 g) with 2.86 g of water. The two solutions were mixed by slowly adding the silica solution into the potassium aluminate one under stirring. After 24 hours of stirring, the precursor mixture was transferred to a Teflon-lined stainless-steel autoclave and heated under static conditions in an oven at 170 °C for 18 h. Finally, the colloidal K-LTL nanocrystals (2.5 wt. %) were purified with water using high-speed centrifugation (RPM 20000, G 37565) until neutral pH is reached.

The ion-exchange of LTL zeolite was carried out directly in the purified colloidal suspensions without drying in order to maintain its colloidal stability of the nanocrystals and prevent irreversible aggregation. The ion-exchanged was performed two times with a 0.03 mM of $Gd(NO_3)\cdot 6H_2O$ solution and 5 ml of 2.5 Wt.% of K-LTL zeolite as described elsewhere[17]. The resulting Gd-exchanged LTL zeolite was purified with water and finally stored in the form of colloidal suspension in aqueous solution.

1.3 Characterization

The crystallinity of the samples was characterized by powder X-ray diffraction (PXRD) using a PANalytical X'Pert Pro diffractometer using Cu Kα1 radiation (λ = 1.5406 Å, 45 kV, 40 mA).

The porosity of the samples was determined by N_2 adsorption/desorption isotherms measured at −196 °C. The O_2 adsorption isotherm on LTL zeolite was measured at 0, 25 and 37 °C using a Micromeritics 3Flex Surface Characterization unit. All samples were degassed at 250 °C under vacuum overnight prior to adsorption analysis. The external surface area and micropore volume were assessed by the t-plot method. The micropore and mesopore size distributions of samples were extracted from the adsorption and desorption branches of the isotherms using the Nonlocal Density Functional Theory (NLDFT) method.

The oxygen adsorption study on nanosized LTL zeolite was performed by *in situ* Fourier-transform infrared (FTIR) spectroscopy suing a Nicolet 6700 IR spectrometer equipped with a mercury cadmium telluride (MCT) detector. The spectra were recorded in the range of 1300–4000 cm^{-1} at a resolution of 4 cm^{-1} after an accumulation of 256 scans. The samples were pressed (~10^7 Pa) into self-supported disks (2 cm^2 area, 20 $mg\cdot cm^{-2}$) and placed in an IR cell equipped with KBr windows. The activation of the zeolite samples was performed *in situ* at 300

°C for 4 h under vacuum and cooled down to –196 °C. Various amounts of pure oxygen gas were introduced into the cell at 0–100 Torr equilibrium pressure. The spectrum of activated zeolite was used as a background for collecting the difference spectra, which were normalized to the sample mass and plotted as absorbance per gram over wavelength.

The surface morphology and the element composition of samples were studied by Scanning electron microscopy (SEM) with energy-dispersive X-ray spectroscopy (EDX) using a Tescan Mira I LMH under 20 kV. The shape and size of nanoparticles were studied by high-resolution transmission electron microscopy (HRTEM) with an FEI Tecnai G2 30 microscope (Vacc = 300 kV, LaB6).

The thermal stability of samples was evaluated by thermogravimetric analysis (TGA) using a TAG24 SETARAM analyzer under a 40 $ml\cdot min^{-1}$ airflow. The measurements were carried out between 25 and 800 °C with a heating rate of 10 $°C\cdot min^{-1}$.

Magic-angle spinning nuclear magnetic resonance (MAS-NMR) experiments of samples were recorded with a single pulse on a Bruker Avance 500 MHz (11.7 T) spectrometer using 4 mm OD zirconia rotors with a spinning frequency of 12 kHz.

The chemical composition of samples was analyzed by inductively coupled plasma mass spectrometry (ICP-MS) using a 7900 ICP-MS from Agilent Technologies. The samples were prepared according to the following procedure: (i) 50 mg of sample was dissolved in 3 mL of hydrofluoric acid (HF) (Sigma-Aldrich 40–45%), then (ii) a 0.5 mL of mixture ($HNO_3/HCl \equiv$ 1:3 v/v) was added and heated at 110 °C for 1 h in the polytetrafluoroethylene (PTFE) bottle (100 mL), and (iii) 96.5 mL of double distillated water and 2 g of boric acid (H_3BO_3) were added. The resulting solution was stirred overnight to facilitate dissolution of the boric acid. Finally, 10 ml of the solution was diluted 10 times with double distillated water before analysis.

The colloidal stability and average size of particles dispersed in water were determined using dynamic light scattering (DLS) performed with a Malvern Zetasizer Nano instrument. The surface charge of the samples was measured by conducting zeta potential measurements of the same suspensions.

1.4 Cell culture and cell viability

The human glioblastoma-derived cell line U251-MG (Cellosaurus_0021) and U87-MG (Cellosaurus_0022) purchased from National Cancer Institute (NCI, Bethesda, MD, USA) and American Type Culture Collection (ATCC, LGC standards, Molsheim, France) respectively, were cultured in DMEM containing 1 g/L of glucose (Dulbecco's Modified Eagle's Medium, Sigma-Aldrich, St Quentin Fallavier, France) supplemented with 10% fetal calf serum (Eurobio, Courtaboeuf, France), 2 mM L-glutamine (Sigma-Aldrich), 100 U/mL penicillin and 100 µg/mL streptomycin (Sigma-Aldrich). The cell line was maintained in culture at 37 °C with 5% CO_2 and 95 % humidity.

Cell viability analyses were performed under exposure to increased concentration of nanosized zeolites for 24 h and 72 h with a WST-1 assay (Roche, Bale, Switzerland) according to the manufacturer's instruction.

1.5 Hemolysis assay

The red blood cells (RBC) were collected from fresh rat blood by centrifugation (1000 rpm, 5 min) and suspended in PBS solution. Then, K-LTL or Gd-LTL zeolite nanoparticles at various concentration were incubated with 500 µL RBC suspension. Saline and 1% Triton X-100 were used as negative and positive controls, respectively. After the incubation at 37 °C for 1 h, the samples were centrifugated (2000 rpm, 10 min) and each supernatant at 540 nm was analysed by a spectrophotometer (Spark®, TECAN, Männedorf, Switzerland). The following formula was used to calculate the percent of hemolysis of RBC.

$$Hemolysis\ (\%) = \frac{Sample\ absorbance - Negative\ control\ absorbance}{Positive\ control\ absorbance - Negative\ control\ absorbance} \times 100$$

1.6 Analysis of oxygen release using LTL nanozeolites

The oxygen release capacity of LTL nanozeolite in aqueous solution was studied in a hypoxia workstation (IN VIVO 2 500, Baker Ruskinn, Alliance Bio Expertise, Guipry, France) set at 0.1% O_2, 5% CO_2 at 37 °C in humidified atmosphere as previously reported [18]. A closed reaction tube containing 12 mL of equilibrated PBS at 0.1% O_2 and 37 °C was used, and a dissolved oxygen sensor (SevenGo (Duo) pro™/OptiOx™, Mettler Toledo, USA) was immersed in the PBS solution. Prior to experiments, baseline was established by measuring the oxygen saturation in the PBS solution for 30 min. Oxygen-saturated nanosized zeolites (500 µL at 1 wt. %) were then added to the system and oxygen dissolved in the PBS solution was measured for 60 min. The oxygen liberation capacity of as prepared and ion-exchanged nanosized zeolites was compared to oxygen-saturated water (used as control).

1.7 Relaxometry measurements

Gd-LTL nanocrystals were dispersed in distilled water at concentration ranging from 0.0625 to 0.001 mM of Gd. Solutions were placed in polypropylene tubes set to a polystyrene support. MRI acquisitions of the phantoms were performed at room temperature on a 7 Tesla BioSpec MRI (Bruker, Ettlingen, Germany). For T1-weighted (T1w) images, a flow sensitive alternating inversion recovery and rapid acquisition with relaxation enhancement (FAIR-RARE) sequence was used (TR: 6000 ms, TE: 77.82 ms, TI: increasing from 25 ms to 5000 ms, RARE factor of 32, image matrix: 128 × 128, 1 slice with a thickness of 3 mm and total acquisition time of 4 min). Image analysis and T1 calculation were performed with Bruker Paravision (version 360.3.3), MATLAB R2021b and ImageJ (version 1.50f). The R1 value (1/T1) was plotted as a function of the Gd concentration and the slope of the line corresponded to the relaxivity ($mM^{-1}\cdot s^{-1}$). In this study 1 mM Dotarem® and water were used as a control samples.

2. Results and discussions

2.1 Physicochemical characterization of LTL nanozeolites

The crystallinity of as-prepared K-LTL and ion-exchanged Gd-LTL zeolites were investigated by powder X-ray diffraction. As it can be seen in **Figure 1a**, the PXRD patterns of the pristine K-LTL and Gd-LTL zeolite samples are identical and exhibit similar peaks being assigned to the LTL-type framework topology[30]. The relatively broad peaks are originating from the small size of the crystals. The average crystallite size is approximately 15 nm, according to Debye-Scherrer equation[31]. Although the LTL zeolite was subjected to an ion-exchange process, no new crystal phase was detected, and the original crystallinity is maintained. Moreover, no shift was observed in peaks positions of Gd-LTL as compared to the pristine material, indicating that the unit cell parameters, as well as particle size, were not altered after the ion-exchange process.

The K-LTL and Gd-LTL zeolite particle's morphology and size were characterized by SEM and TEM. According to the SEM (**Figure 1b**), both K-LTL and Gd- LTL consist of well-defined small nanocrystals. After the ion-exchange process, no significant changes were observed. The chemical compositions of the K-LTL and Gd-LTL are obtained by EDX spectrometry (**Figure S1 and Figure 1c**). The EDX results confirm that potassium was only partially exchanged by gadolinium. Such behavior is not surprising since, potassium ions in K_1 and K_2 sites are very stable (**Figure S2**) [28,29,32].

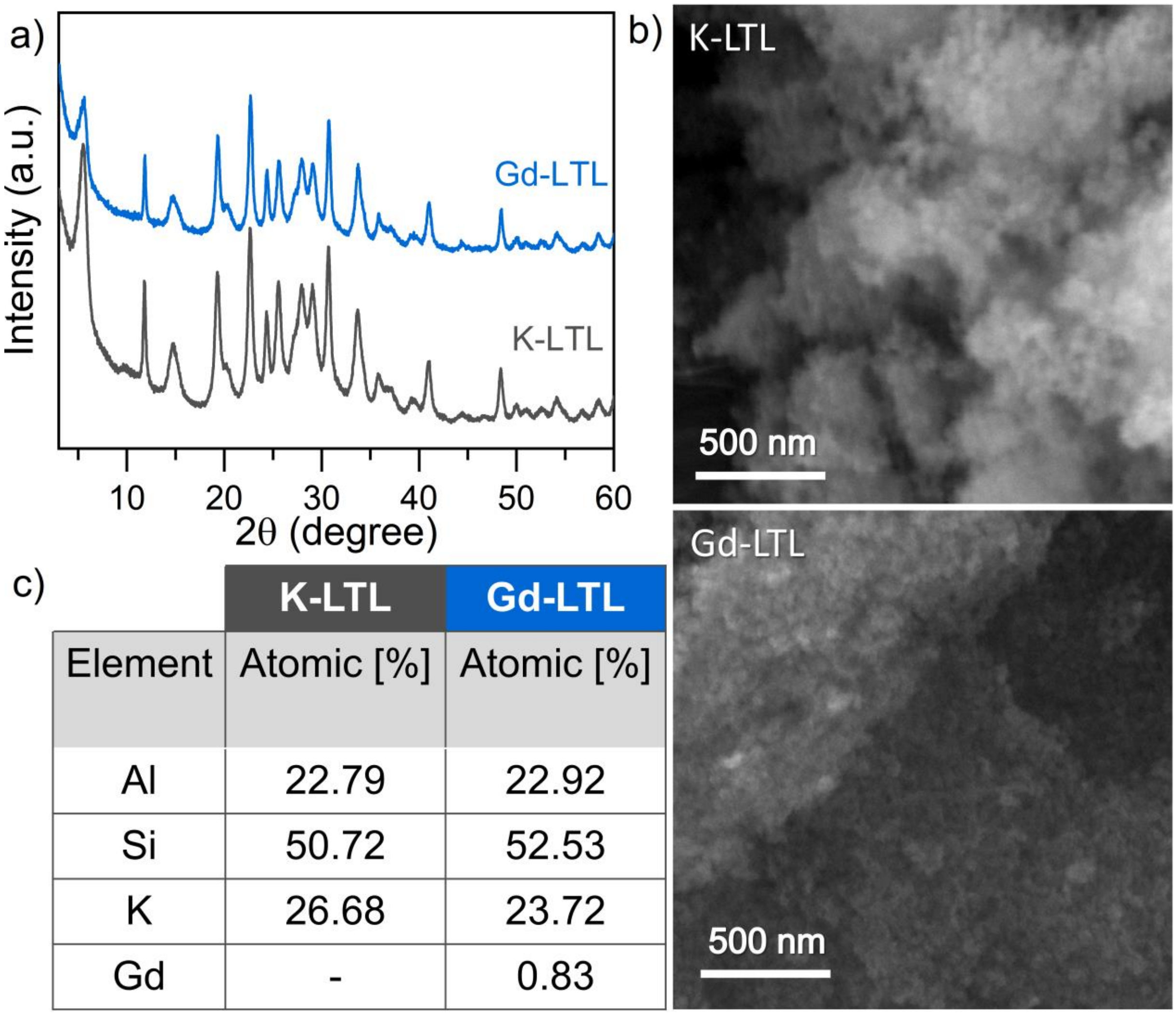

	K-LTL	Gd-LTL
Element	Atomic [%]	Atomic [%]
Al	22.79	22.92
Si	50.72	52.53
K	26.68	23.72
Gd	-	0.83

Figure 1. a) Powder X-ray diffraction patterns b) SEM and c) chemical composition of K-LTL and Gd-LTL nanosized zeolites determined by EDX.

The HR-TEM observations show a uniform distribution of well-defined nanocrystals with a high crystallinity. Moreover, HR-TEM showed that LTL particles exhibited elongated cylindrical shape of size of 10 x 20 nm (**Figure 2**). Since it is of particular importance for the targeted applications, the particle size distribution as well as the colloidal stability of the water suspensions containing K-LTL and Gd-LTL were studied by DLS (**Figure 3**). The mean hydrodynamic diameter of particles obtained by DLS is 15 nm. The hydrodynamic size of the nanoparticles remained stable with no variations with time, making them well-suited for *in vivo* applications. The zeta potential values of K-LTL and Gd-LTL colloidal suspensions are -46 and

-48 mV, respectively, confirming proper colloidal stability and negatively surface charged particles.

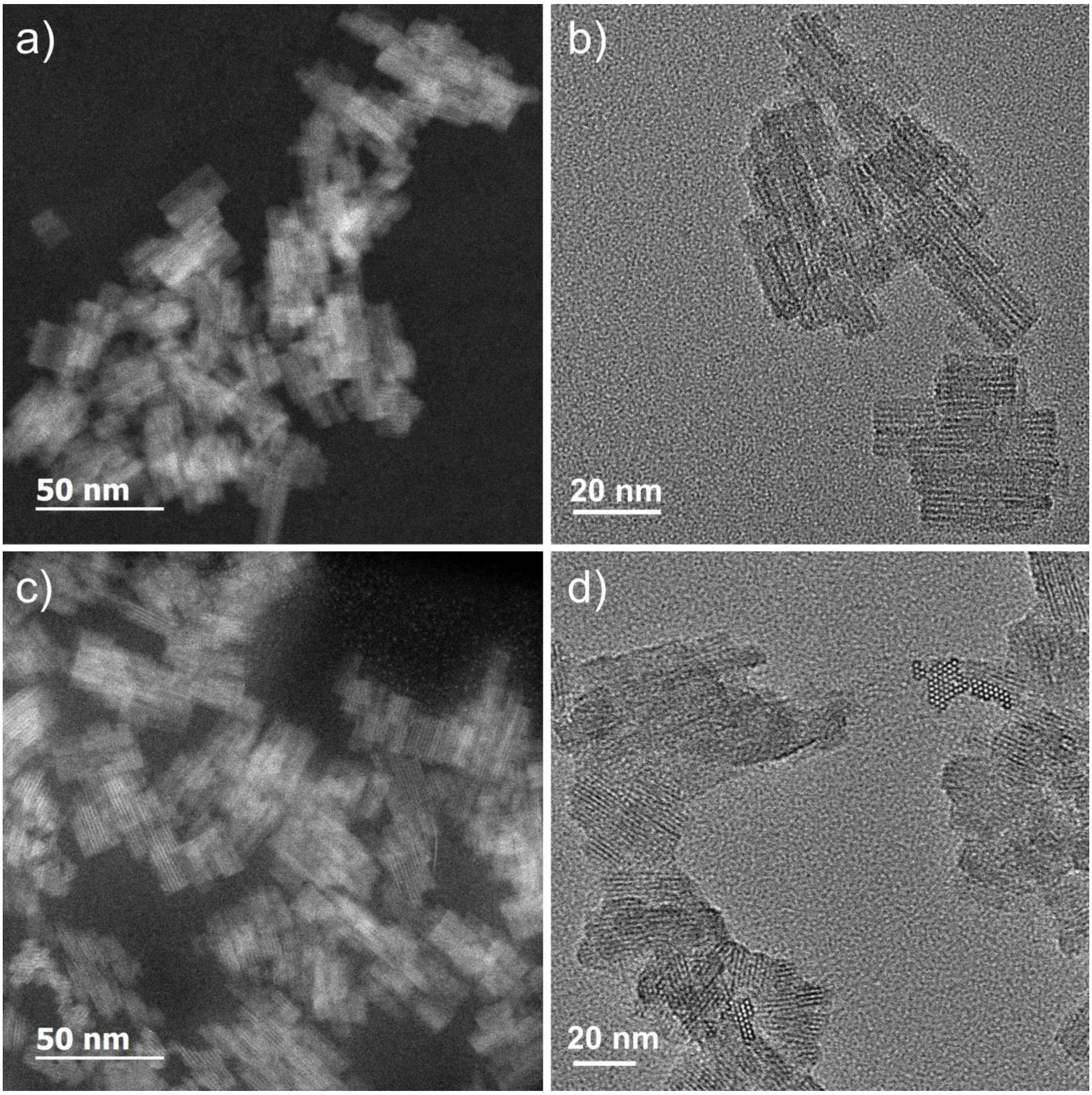

Figure 2. HAADF–STEM images of (a, b) K-LTL and (c, d) Gd-LTL nanosized zeolites at different magnifications.

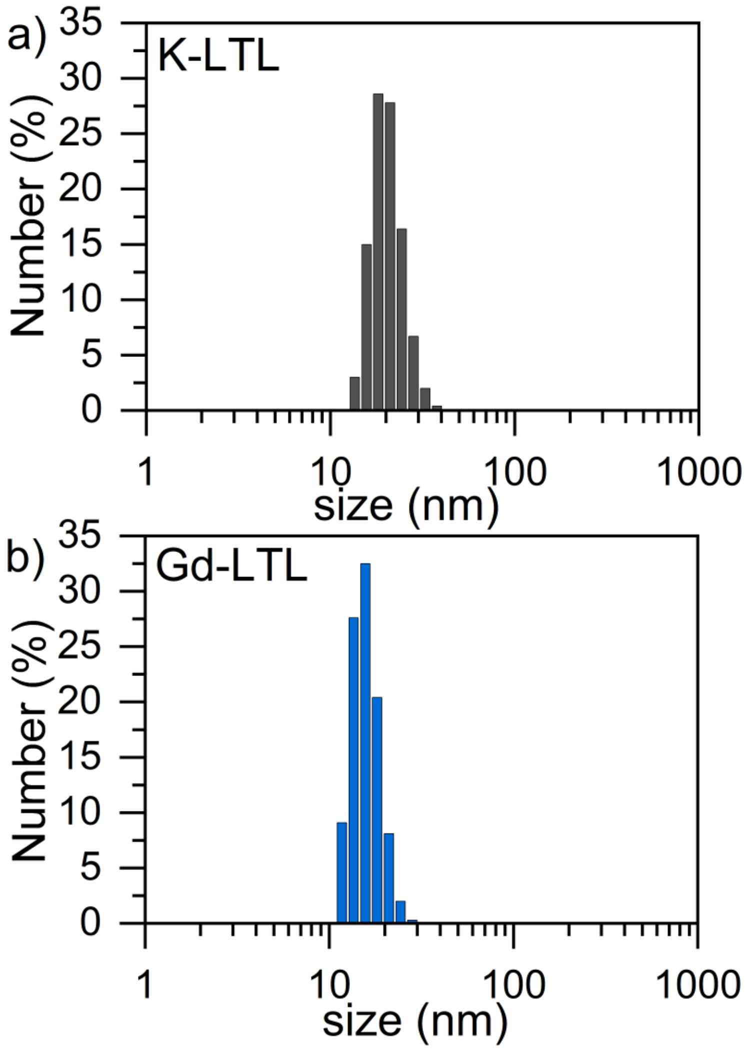

Figure 3. Dynamic light scattering profile of a) K-LTL and b) Gd-LTL nanosized zeolites.

Both K-LTL and Gd-LTL samples contain only one thermal decomposition step in the TG/DTG curves caused by the removal of water present in the crystals (**Figure 4a-b**). For both samples, the temperature corresponding to the complete water removal is 244 °C and the total water content is about 15%. Similar results were also obtained by Gigli *et al.* and the mechanism of dehydration was discussed earlier [33]. Interestingly, the ion-exchange process of nanosized LTL samples did not alter their hydrophilicity. The chemical compositions of samples are determined by combining the ICP-MS elemental analysis with TG results. The stoichiometric chemical composition of the samples is $|K_{10.38}(H_2O)_{24.92}|$ $[Si_{26.80}Al_{10.35}O_{72}]$ (Si/Al = 2.59) and $|K_{9.77}Gd_{0.34}(H_2O)_{24.13}|$ $[Si_{25.80}Al_{10.24}O_{72}]$ (Si/Al = 2.52) for K-LTL and Gd-LTL, respectively. The amount of gadolinium loaded in LTL zeolite is about 1.53 wt.%, which corresponds to

~0.34 Gd^{3+} ions per unit cell. The chemical composition of the samples is presented in **Table 1**. The results show that potassium is only partially exchanged with gadolinium.

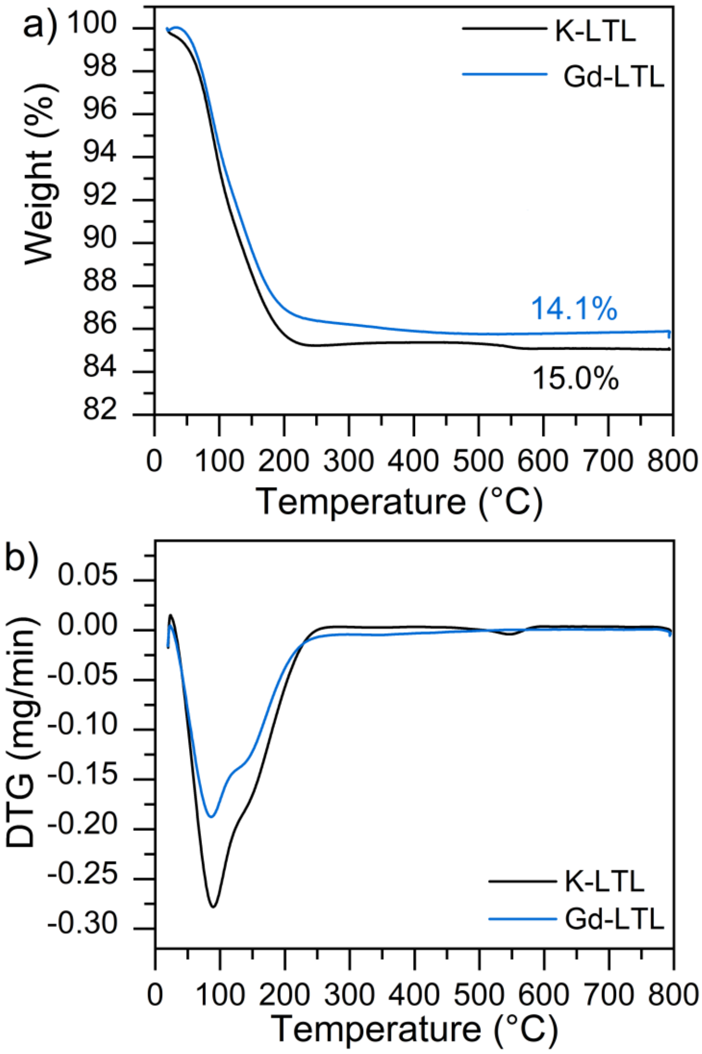

Figure 4. a) TG and b) DTG curves of K-LTL and Gd-LTL nanosized zeolites

The K-LTL and Gd-LTL were further subjected to FT-IR and MAS-NMR spectroscopy characterization. The characteristic structural bands of K-LTL and Gd-LTL are relatively identical **(Figure 5a)**. The IR broad absorption bands centered at 3441 and 1633 cm^{-1}, were attributed to the stretching and bending vibrations mode of adsorbed water molecules in the zeolite samples, respectively[34]. The most intense bands located at 1101 and 1119 cm^{-1} are characteristic of the asymmetric stretching frequencies of Si-O-Si and Si-O-Al groups units i.e. SiO_4 and AlO_4 tetrahedra in zeolites[34]. The bands at 762 and 724 cm^{-1} correspond to symmetric stretching vibrations of Si-O-Al-O-T (T = Si or Al) and the band centered at 458 cm^{-1} is attributed to bending vibrations[35]. The Si/Al ratio of the zeolite samples is also calculated using FTIR data according to reference [36] (**Table 1**). In addition, the isolated silanols (Si-OH) for K-LTL and Gd-LTL were studied after activation of the samples at 300 °C (**Figure 5b**). Both samples contain bands in the range of 3765–3505 cm^{-1}, which are typical of isolated external silanol groups. These bands have a high relative intensity because of the small crystal size, which has already been identified as a spectral characteristic of nanosized zeolites with well-developed external surface area [37].

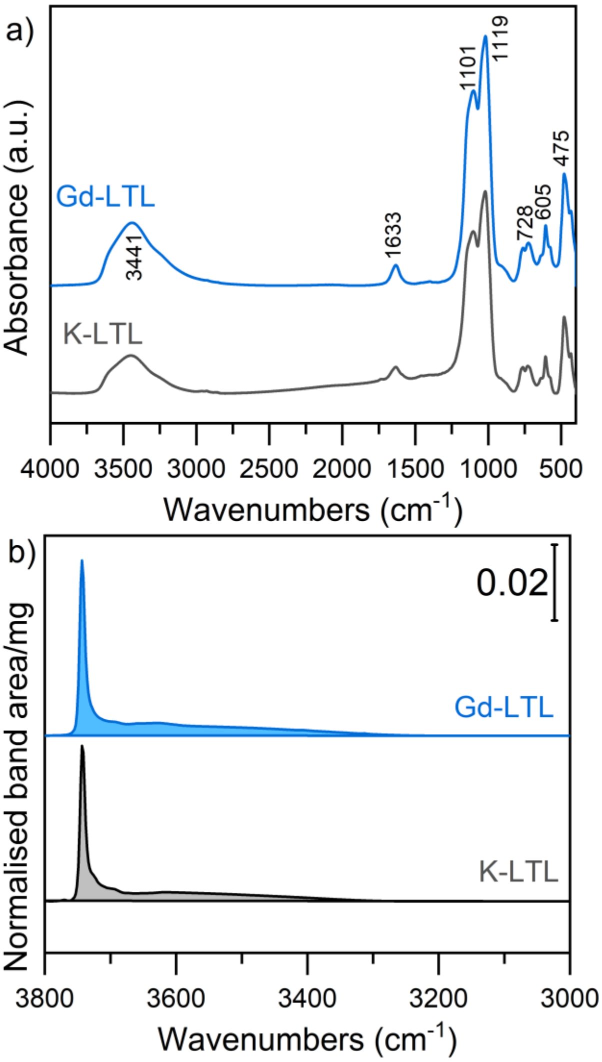

Figure 5. IR spectra a) using KBr technique in the range 400-4000 cm^{-1} and b) using self-supported pallet in the range 3000-3800 cm^{-1} of K-LTL and Gd-LTL nanosized zeolites

Table 1. Elemental composition of K-LTL and Gd-LTL nanosized zeolites determined by ICP, EDX, NMR and FTIR.

Sample	**Chemical composition (wt. %)**							
	K	**Si**	**Al**	**Gd**	**Si/Al ICP**	**Si/Al EDX**	**Si/Al NMR**	**Si/Al FTIR**
K-LTL	11.81	22.45	8.65	-	2.59	2.22	2.52	3.13
Gd-LTL	10.76	20.42	7.79	1.53	2.52	2.29	2.47	3.08

The solid-state ^{29}Si and ^{27}Al NMR spectra of K-LTL and Gd-LTL samples are shown in **Figure 6a-d**. The spectra of both samples show broad peaks convoluted in five peaks at - 84, -90, -96, -100, and -105 attributed to Q0 (4Al), Q1 (3Al), Q2 (2Al), Q3 (1Al), and Q4 (0Al) species, respectively. The Si/Al ratio of the samples is determined by the Engelhardt equation from the deconvolved ^{29}Si MAS NMR spectra. The Si/Al ratio for K-LTL and Gd-LTL is 2.52 and 2.47, respectively. The ^{27}Al MAS NMR spectra reveal a single resonance peak at 60 ppm, thus confirming that no extra-framework aluminum both K-LTL and Gd-LTL is present.

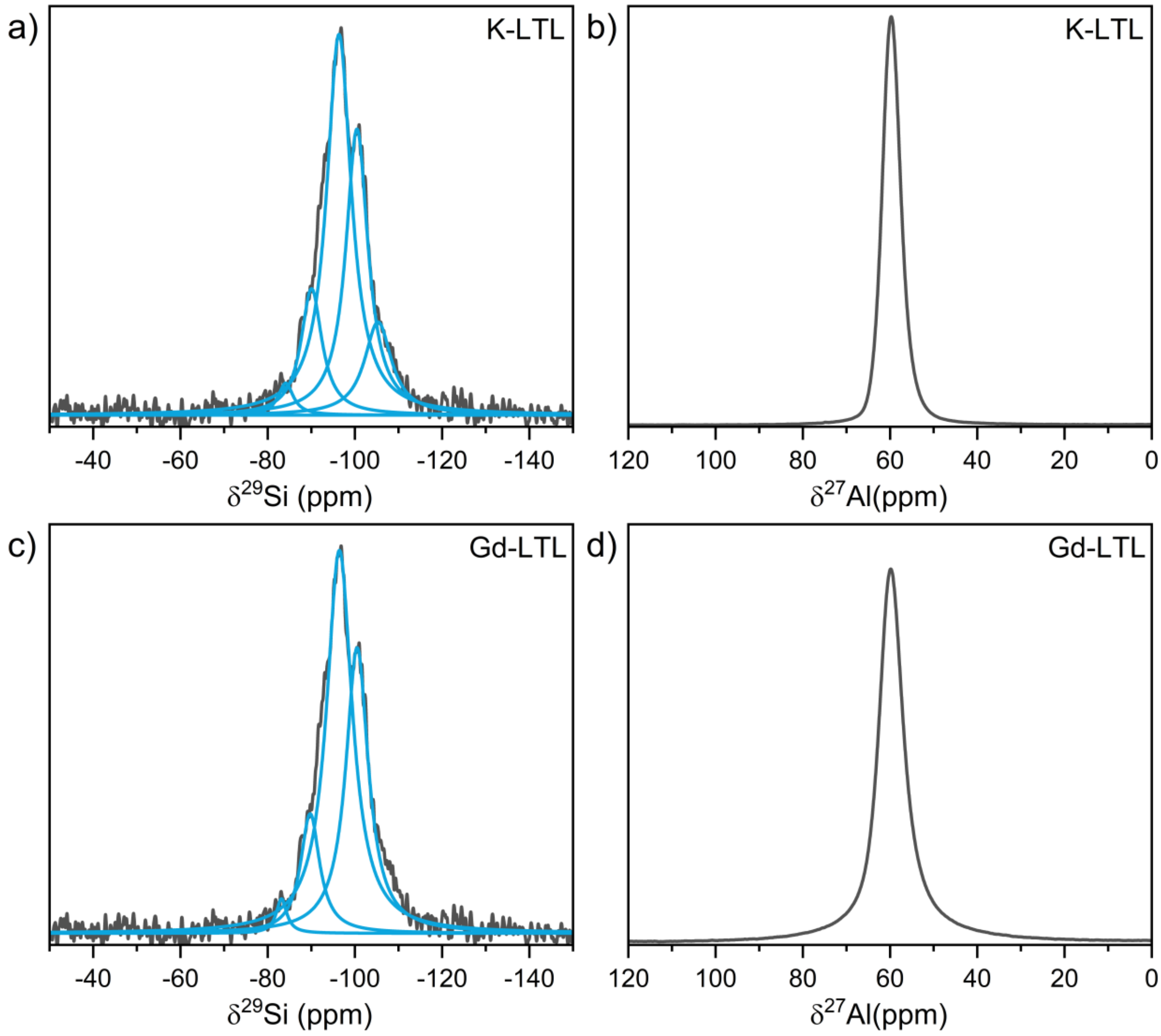

Figure 6: a) ^{29}Si and b) ^{27}Al MAS NMR spectra of K-LTL and c) ^{29}Si and d) ^{27}Al MAS NMR spectra of the Gd-LTL nanosized zeolites.

The porosity of zeolite nanocrystals was further investigated by nitrogen adsorption-desorption measurements. The nitrogen adsorption isotherms and the corresponding pore size distribution are shown in **Figure 7a-b**; the textural parameters are summarized in **Table 2**. Both samples display hybrid type I and IV isotherms, according to the IUPAC classification[38]. Such isotherms are typically observed for monodisperse microporous nanoparticles. In addition, both materials exhibit a H1-type hysteresis loop. The mesoporosity is originating from the interparticle voids. The Brunauer-Emmett-Teller surface area for K-LTL and Gd-LTL samples is 591 and 546 m^2/g, and the total pore volume is 0.76 and 0.81 cm^3/g, respectively (**Figure 7a-b)**. Both samples exhibit the same micropore volume of 0.14 cm^3/g. In addition, the pore size distribution for both samples is calculated with a NLDFT model (**Figure 7b)**. The results confirmed that K-LTL and Gd-LTL samples exhibit one family of supermicropore ($0.7<w<2$ nm) with an average size of 0.75 nm which is in accordance with the mono-dimensional channel system[27] in LTL zeolite and the presence of mesopores with a size of 2-15 nm.

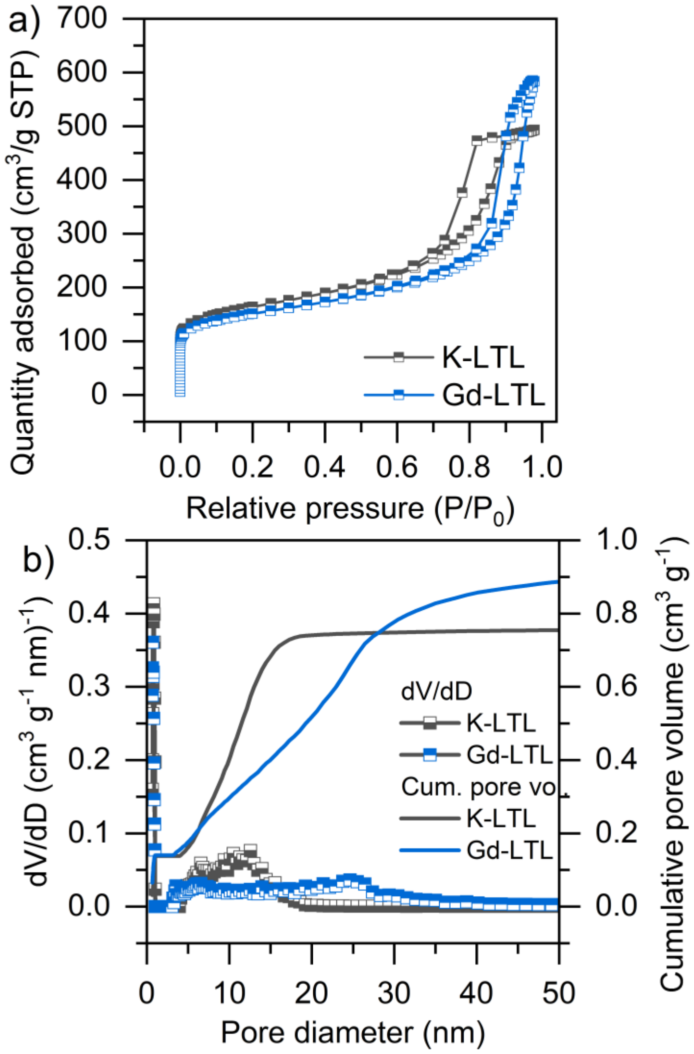

Figure 7. a) Nitrogen adsorption/desorption isotherms and b) NLDFT pore size distribution and the cumulative pore volume of K-LTL and Gd-LTL nanosized zeolites.

Table 2. Properties of K-LTL and Gd-LTL nanosized zeolites determined by N_2 adsorption characterization

Sample	Surface area S_{BET} (m^2/g)	Total Pore volume (cm^3/g)	NLDFT Micro Pore volume (cm^3/g)	NLDFT pore size (nm)
K-LTL	591	0.76	0.14	0.8
Gd-LTL	546	0.81	0.14	0.7

2.2 Assessment of potential toxicity of LTL nanozeolites

To assess the biocompatibility of LTL nanozeolites as oxygen-carrier or contrast agent, cytotoxicity measurements were performed on different human cell lines. U251-MG and U87-MG cells were exposed to as-prepared and ion-exchanged nanosized zeolites at concentrations of 10 or 100 µg/mL for 24 h and 72 h, followed by cell viability measurements. As shown in **Figure 8**, the U251-MG and U87-MG cell viability was not modified by exposure to both K-LTL and Gd-LTL nanosized zeolites. Our results clearly show the absence of acute toxicity of the nanocrystals on glioblastoma cell lines.

The evaluation of hemocompatibility of nanoparticles is an important point to be considered prior using for in vivo applications. In this study, the hemocompatibility of LTL nanoparticles was evaluated with hemolysis assay using rat blood incubated with variable concentrations of zeolite nanoparticles [10 to 500 µg/mL]. As shown in **Figure 8e**, the incubation of blood with K-LTL or Gd-LTL zeolite nanocrystals for 1 h resulted in a maximum hemolytic ratio of 0.942 ± 0.771 % and 0.722 ± 0.401 %, respectively for the highest concentration. These results clearly showed an absence of toxicity of nanozeolites to RBC. Indeed, the hemolysis rate of the samples is less than 5%, which is considered as a safe critical value for biomaterials according to the ISO/TR 7406.

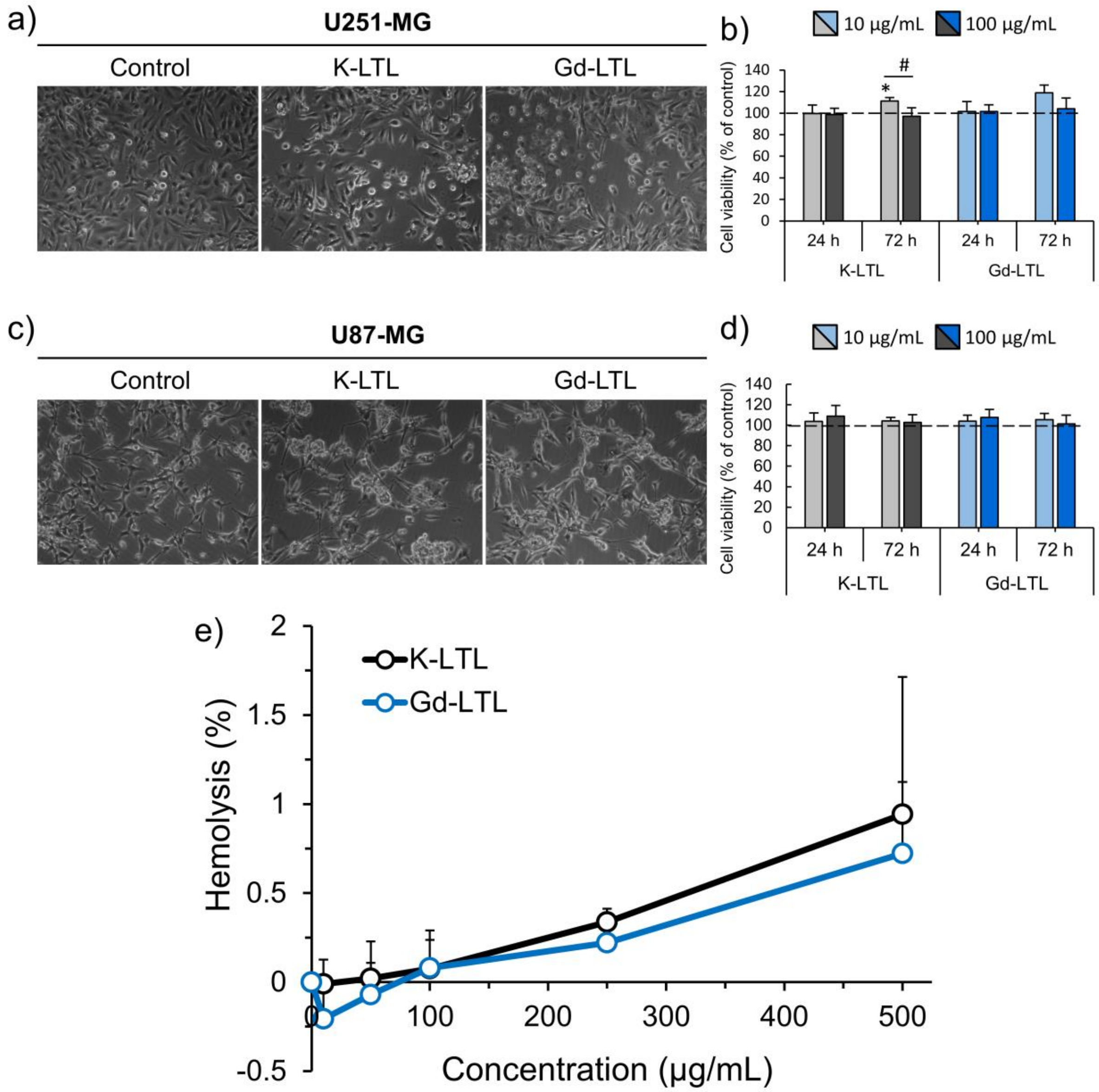

Figure 8. Cell viability of human glioblastoma-derived cell lines exposed to K-LTL and Gd-LTL zeolite nanocrystals. Representative phase contrast photographs of a) U251-MG and b) U87-MG cells after 72 h exposure to 100 µg/mL of K-LTL and Gd-LTL zeolite nanocrystals and a control (H_2O). Quantification of a) U251-MG and d) U87-MG viability after 24 and 72 h exposed to increasing concentrations of K-LTL and Gd-LTL zeolites. Cell viability was assessed using the WST-1 assay. Mean ± SD, N=5, $^{*}p < 0.05$ *vs* control, $^{\#}p < 0.05$ *vs* 10 µg/mL, Kruskall-Wallis test, e) Hemolysis assay for K-LTL (black), Gd-LTL (blue) nanozeolites incubated with rat RBCs with concentrations 10, 50, 100, 250 and 500 µg/mL at 37 °C for 1 h. Mean ± SD, n=3 independent experiments.

2.3 Oxygen adsorption capacity of LTL nanozeolites

The equilibrium adsorption isotherms of oxygen on nanosized K-LTL and Gd-LTL zeolites at different temperatures are depicted in **Figure 9a-b**. The amount of O_2 (100 kPa) adsorbed on nanosized K-LTL zeolites at 0, 25 and 37 °C is 5.27 cm^3g^{-1}, 3.53 $cm^3g^{-1,}$ and 3.09 cm^3g^{-1}, respectively. As expected, the amount adsorbed oxygen decreases with the temperature. The nanosized K-LTL has a high oxygen adsorption capacity compared to the reported values for micron-sized LTL zeolites of 2.3 cm^3 g^{-1} (100 KPa, 25 °C) and for commercial faujasite zeolite X of 2.96 cm^3 g^{-1} (100 KPa, 37 °C)[39,40]. This can be due to the different chemical composition and diffusion paths in nanosized zeolites It is also proposed that the oxygen molecules interact primarily with the zeolite through its Brønsted acid sites and extra-framework cations. Therefore, when K^+ cations are partially ion-exchanged with trivalent Gd^{3+}, the O_2 adsorption capacities increases. For Gd-LTL, the O_2 capacities at 0, 25 and 37 °C is found to be 5.78 cm^3g^{-1}, 4.60 $cm^3g^{-1,}$ and 3.71 cm^3g^{-1} respectively. The overall increase in the adsorption capacity is attributed to the removal of K^+ cations. Indeed, when one trivalent cation is introduced, three K^+ cations are removed, thus creating additional space and lead to improved accessibility of oxygen molecules.

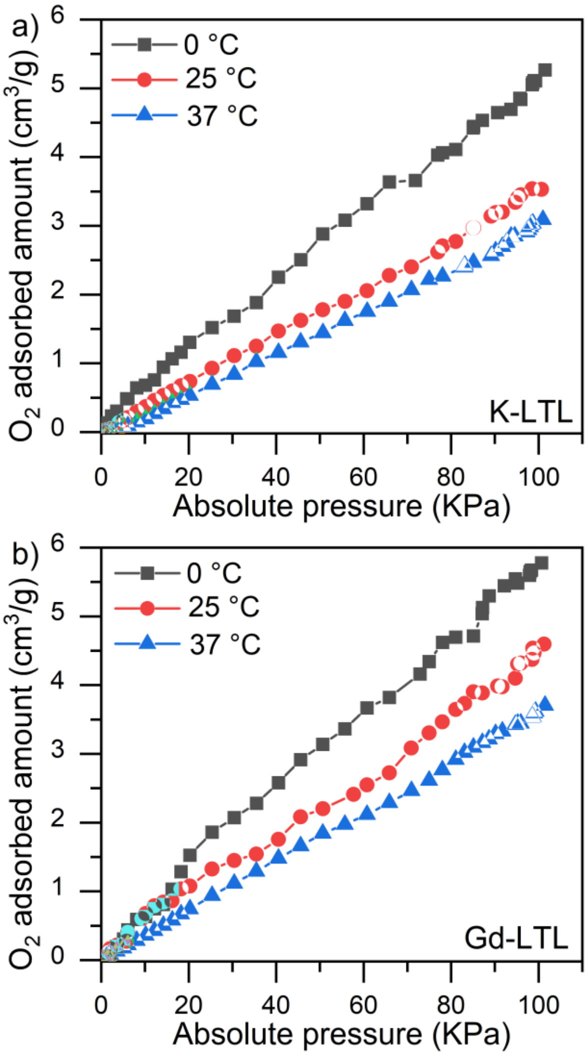

Figure 9. Oxygen adsorption isotherms of a) K-LTL and b) Gd-LTL nanosized zeolites at different temperatures

To further confirm the volumetric adsorption results, the adsorption of oxygen on LTL zeolites was also investigated by *in situ* FTIR at -196 °C exposed to different oxygen pressures and the results are shown in **Figure S3**. The IR spectra of both samples under adsorption of O_2 show strong absorption band centered at 1552 cm^{-1} characteristics to the interaction of oxygen molecules with K^+ sites for K-LTL and K^+, Gd^{3+} for sample Gd-LTL and consequently, this alteration of its symmetry prevents any IR band from being detected in its gas phase. Since oxygen is a nonpolar molecule, the small shift of the peak located at 1553 cm^{-1} with increasing oxygen pressure reflects a weak bonding [41]. The total interaction energy of the physical adsorption of these molecules on zeolites includes contributions from dispersion, close-range repulsion, polarization and field−quadrupole [40]. The introduction of the Gd^{3+} cations is found to improve the O_2 sorption capacity of LTL nanosized zeolite by 27% as shown in **Figure 10a**. In addition, the intensity of the oxygen band does not change significantly over several sorption cycles, indicating that the LTL zeolite maintains the O_2 capacity after several cycles.

One of the most important property of gas (oxygen) delivery bio-vectors for tumor oxygenation, is the ability to release the oxygen molecules over an appropriate time period. Therefore, the oxygen release from an oxygenated K-LTL and Gd-LTL nanozeolite using a dissolved oxygen probe under hypoxic conditions was studied. A maximum O_2 release after 6 min and 8 min using K-LTL ($\sim 1.56\ mg \cdot L^{-1}$) and Gd-LTL ($\sim 2.18\ mg \cdot L^{-1}$), respectively was observed **Figure 10b**. Afterwards, the oxygen concentration showed a slow decrease over time due to the diffusion of O_2 into the air. The above results indicated that our materials have the ability to adsorb and release of oxygen in liquid media.

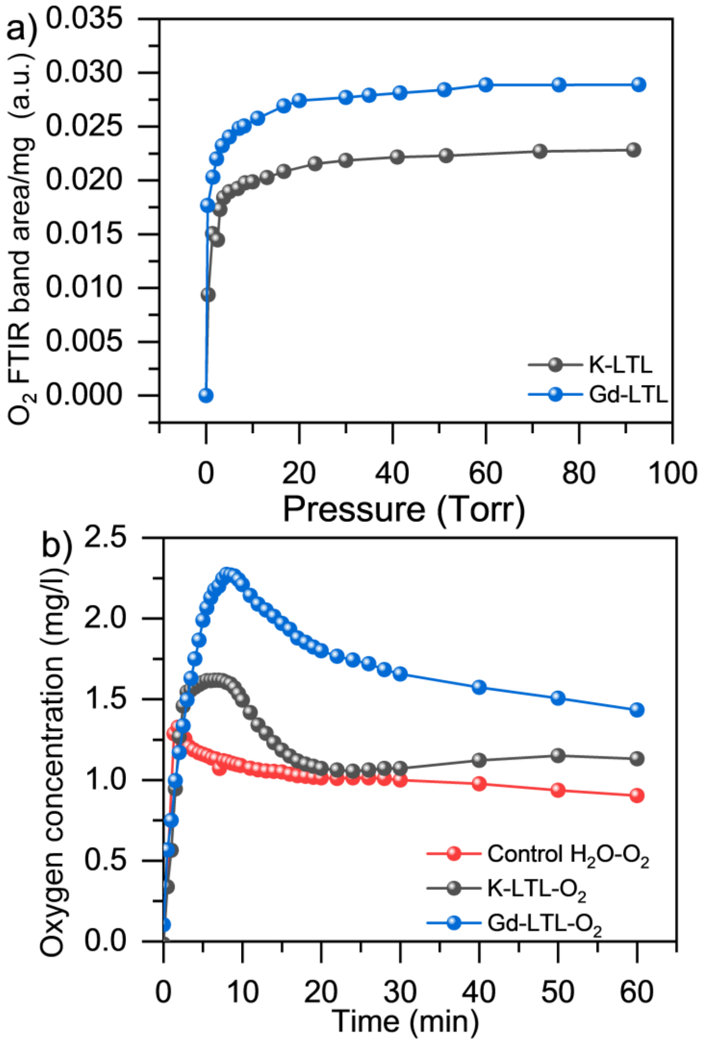

Figure 10. a) FTIR band area normalized to the mass of K-LTL and Gd-LTL nanosized zeolites as a function of O_2 pressures and b) time-dependent changes of oxygen concentration in PBS solution with addition of oxygen-saturated K-LTL and Gd-LTL nanosized zeolites and the control sample (oxygen-saturated water).

2.4 Magnetic resonance imaging proprieties of LTL nanozeolites

MRI is a vital imaging technique widely used in clinical imaging modality due to its ability to provide high soft tissue contrast and penetrate deep into the body. Gd^{3+} ions in the LTL nanosized zeolite are promising candidates for use as contrast agents in MRI. It will shorten the longitudinal (T1) relaxation of protons, resulting in an increase of signal intensity and bright contrast in regions where the contrast agent accumulates in T1-Weighted imaging. To assess the strength of the contrast agent, it is convenien to obtain T1 map as a function of Gd concentration and then to compute the resulting r1 (relaxivity expressed as mM^{-1} s^{-1}).

Figure 11a shows greyscale coded T1 maps of Gd-LTL at increasing Gd concentrations (0.001 - 0.0625 mM). T1 mapping shows noticeable shortening of the T1 values with increasing the Gd concentration. The resulting r1 (1/T1) value of Gd-LTL calculated at 7 Tesla at room temperature was 79 $mM^{-1}\ s^{-1}$ (**Figure 11b**). The obtained value of r1 was 20 times higher than those of commercial Gd-chelates (e.g., the relaxivity induced by Dotarem® Gd-DOTA or Magnevist® Gd-DTPA is at about 4 $mM^{-1}\ s^{-1}$ at 7T)[42,43].

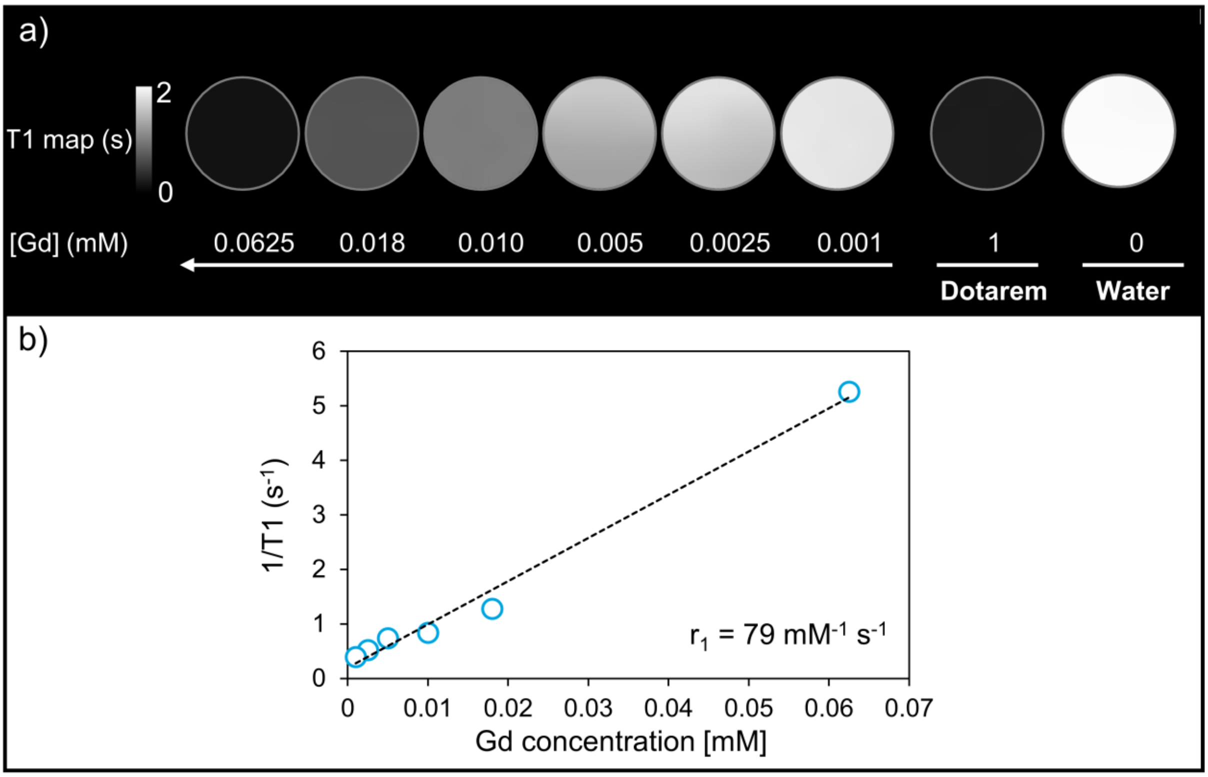

Figure 11. a) T1 map MR images as a function of Gd(III) ion concentration and b) Plots of the R1 value (1/T1) as a function of Gd(III) ion concentration. Slope provide r1 value

3. Conclusions

The synthesis of non-toxic nanosized LTL zeolites containing either K or Gd as extra framework cations for oxygen delivery in hypoxic media and MRI imaging are reported. The ability of LTL nanosized zeolite to adsorb and release O_2 under hypoxic conditions is demonstrated. The results show that the Gd-LTL nanosized zeolite exhibits an oxygen capacity of 5.27 cm^3/g and shows the highest O_2 release in the hypoxic medium. Importantly, the incorporation of Gd in the LTL zeolite enabling MRI tracking and preserved structural, textural, colloidal and morphological properties of the nanosized crystals. The toxicity experiments using glioblastoma cell lines demonstrate the non-toxic behavior of the LTL nanosized zeolites.

Acknowledgments

The financial support from the Conseil Régional de Normandie, FEDER Program Zeoxy, INCA (INCA 11699), CNRS Innovation and the Centre of zeolites and nanoporous materials, Region Normandie, CNRS (CLEAR) is acknowledged.

References

(1) Gallego, E. M.; Paris, C.; Díaz-Rey, M. R.; Martínez-Armero, M. E.; Martínez-Triguero, J.; Martínez, C.; Moliner, M.; Corma, A. Simple Organic Structure Directing Agents for Synthesizing Nanocrystalline Zeolites. *Chem. Sci.* **2017**, *8* (12), 8138–8149. https://doi.org/10.1039/C7SC02858J.

(2) Moliner, M.; Martínez, C.; Corma, A. Multipore Zeolites: Synthesis and Catalytic Applications. *Angew. Chemie Int. Ed.* **2015**, *54* (12), 3560–3579. https://doi.org/10.1002/ANIE.201406344.

(3) Khodadadi Yazdi, M.; Zarrintaj, P.; Hosseiniamoli, H.; Mashhadzadeh, A. H.; Saeb, M. R.; Ramsey, J. D.; Ganjali, M. R.; Mozafari, M. Zeolites for Theranostic Applications. *J. Mater. Chem. B* **2020**, *8* (28), 5992–6012. https://doi.org/10.1039/D0TB00719F.

(4) Zeng, X.; Hu, X.; Song, H.; Xia, G.; Shen, Z. Y.; Yu, R.; Moskovits, M. Microwave Synthesis of Zeolites and Their Related Applications. *Microporous Mesoporous Mater.* **2021**, *323*, 111262. https://doi.org/10.1016/J.MICROMESO.2021.111262.

(5) Wang, X.; Ma, Y.; Wu, Q.; Wen, Y.; Xiao, F. S. Zeolite Nanosheets for Catalysis. *Chem. Soc. Rev.* **2022**, *51* (7), 2431–2443. https://doi.org/10.1039/D1CS00651G.

(6) Mintova, S.; Jaber, M.; Valtchev, V. Nanosized Microporous Crystals: Emerging Applications. *Chem. Soc. Rev.* **2015**, *44* (20), 7207–7233. https://doi.org/10.1039/C5CS00210A.

(7) Database of Zeolite Structures http://www.iza-structure.org/databases/ (accessed Jun 26, 2021).

(8) Serati-Nouri, H.; Jafari, A.; Roshangar, L.; Dadashpour, M.; Pilehvar-Soltanahmadi, Y.; Zarghami, N. Biomedical Applications of Zeolite-Based Materials: A Review. *Mater. Sci. Eng. C* **2020**, *116*, 111225. https://doi.org/10.1016/J.MSEC.2020.111225.

(9) Awala, H.; Gilson, J. P.; Retoux, R.; Boullay, P.; Goupil, J. M.; Valtchev, V.; Mintova, S. Template-Free Nanosized Faujasite-Type Zeolites. *Nat. Mater. 2014 144* **2015**, *14* (4), 447–451. https://doi.org/10.1038/nmat4173.

(10) Ng, E.-P.; Chateigner, D.; Bein, T.; Valtchev, V.; Mintova, S. Capturing Ultrasmall EMT Zeolite from Template-Free Systems. *Science (80-.).* **2012**, *335* (6064), 70–73. https://doi.org/10.1126/SCIENCE.1214798.

(11) Grand, J.; Barrier, N.; Debost, M.; Clatworthy, E. B.; Laine, F.; Boullay, P.; Nesterenko, N.; Dath, J. P.; Gilson, J. P.; Mintova, S. Flexible Template-Free RHO Nanosized Zeolite for Selective CO2Adsorption. *Chem. Mater.* **2020**, *32* (14), 5985–5993. https://doi.org/10.1021/ACS.CHEMMATER.0C01016/ASSET/IMAGES/LARGE/CM0C01016_0008.JPEG.

(12) Mintova, S.; Gilson, J.-P.; Valtchev, V. Advances in Nanosized Zeolites. https://doi.org/10.1039/c3nr01629c.

(13) Wang, Y.; Wu, Q.; Meng, X.; Xiao, F. S. Insights into the Organotemplate-Free Synthesis of Zeolite Catalysts. *Engineering* **2017**, *3* (4), 567–574. https://doi.org/10.1016/J.ENG.2017.03.029.

(14) Georgieva, V.; Vicente, A.; Fernandez, C.; Retoux, R.; Palč, A.; Valtchev, V.; Mintova, S. Control of Na-EMT Zeolite Synthesis by Organic Additives. **2015**. https://doi.org/10.1021/acs.cgd.5b00071.

(15) Georgieva, V.; Anfray, C.; Retoux, R.; Valtchev, V.; Valable, S.; Mintova, S. Iron Loaded EMT Nanosized Zeolite with High Affinity towards CO2 and NO. *Microporous Mesoporous Mater.* **2016**, *232*, 256–263. https://doi.org/10.1016/J.MICROMESO.2016.06.015.

(16) Mintova, S.; Grand, J.; Valtchev, V. Nanosized Zeolites: Quo Vadis? *Comptes Rendus Chim.* **2016**, *19* (1–2), 183–191. https://doi.org/10.1016/J.CRCI.2015.11.005.

(17) Komaty, S.; Daouli, A.; Badawi, M.; Ment Anfray, C.; Zaarour, M.; Valable, S.; Mintova, S. Incorporation of Trivalent Cations in NaX Zeolite Nanocrystals for the Adsorption of O2 in the Presence of CO2. *Phys. Chem. Chem. Phys* **2020**, *22*, 9934.

https://doi.org/10.1039/d0cp00111b.

(18) Anfray, C.; Komaty, S.; Corroyer-Dulmont, A.; Zaarour, M.; Helaine, C.; Ozcelik, H.; Allioux, C.; Toutain, J.; Goldyn, K.; Petit, E.; Bordji, K.; Bernaudin, M.; Valtchev, V.; Touzani, O.; Mintova, S.; Valable, S. Nanosized Zeolites as a Gas Delivery Platform in a Glioblastoma Model. *Biomaterials* **2020**, *257*, 120249. https://doi.org/10.1016/J.BIOMATERIALS.2020.120249.

(19) Komaty, S.; Özçelik, H.; Zaarour, M.; Ferre, A.; Valable, S.; Mintova, S. Ruthenium Tris(2,2′-Bipyridyl) Complex Encapsulated in Nanosized Faujasite Zeolite as Intracellular Localization Tracer. *J. Colloid Interface Sci.* **2021**, *581*, 919–927. https://doi.org/10.1016/J.JCIS.2020.08.117.

(20) Amorim, R.; Vilaça, N.; Martinho, O.; Reis, R. M.; Sardo, M.; Rocha, J.; Fonseca, A. M.; Baltazar, F.; Neves, I. C. Zeolite Structures Loading with an Anticancer Compound as Drug Delivery Systems. *J. Phys. Chem. C* **2012**, *116* (48), 25642–25650. https://doi.org/10.1021/JP3093868/ASSET/IMAGES/LARGE/JP-2012-093868_0010.JPEG.

(21) Zheng, L.; Zhang, Y.; Lin, H.; Kang, S.; Li, Y.; Sun, D.; Chen, M.; Wang, Z.; Jiao, Z.; Wang, Y.; Dai, B.; Zhuang, S.; Zhang, D. Ultrasound and Near-Infrared Light Dual-Triggered Upconversion Zeolite-Based Nanocomposite for Hyperthermia-Enhanced Multimodal Melanoma Therapy via a Precise Apoptotic Mechanism. *ACS Appl. Mater. Interfaces* **2020**, *12* (29), 32420–32431. https://doi.org/10.1021/ACSAMI.0C07297/ASSET/IMAGES/LARGE/AM0C07297_0006.JPEG.

(22) Zhang, W.; Martinelli, J.; Peters, J. A.; Van Hengst, J. M. A.; Bouwmeester, H.; Kramer, E.; Bonnet, C. S.; Szeremeta, F.; Tóth, É.; Djanashvili, K. Surface PEG Grafting Density Determines Magnetic Relaxation Properties of Gd-Loaded Porous Nanoparticles for MR Imaging Applications. *ACS Appl. Mater. Interfaces* **2017**, *9* (28), 23458–23465. https://doi.org/10.1021/ACSAMI.7B05912/ASSET/IMAGES/LARGE/AM-2017-05912J_0005.JPEG.

(23) Mayer, F.; Zhang, W.; Brichart, T.; Tillement, O.; Bonnet, C. S.; Tóth, É.; Peters, J. A.; Djanashvili, K. Nanozeolite-LTL with GdIII Deposited in the Large and Eu III in the Small Cavities as a Magnetic Resonance Optical Imaging Probe. *Chem. - A Eur. J.* **2014**, *20* (12), 3358–3364. https://doi.org/10.1002/CHEM.201304457.

(24) Horsman, M. R.; Mortensen, L. S.; Petersen, J. B.; Busk, M.; Overgaard, J. Imaging Hypoxia to Improve Radiotherapy Outcome. *Nat. Rev. Clin. Oncol. 2012 912* **2012**, *9* (12), 674–687. https://doi.org/10.1038/nrclinonc.2012.171.

(25) Liu, Y.; Jiang, Y.; Zhang, M.; Tang, Z.; He, M.; Bu, W. Modulating Hypoxia via Nanomaterials Chemistry for Efficient Treatment of Solid Tumors. *Acc. Chem. Res.* **2018**, *51* (10), 2502–2511. https://doi.org/10.1021/ACS.ACCOUNTS.8B00214/ASSET/IMAGES/LARGE/AR-2018-00214H_0007.JPEG.

(26) Price, L. A.; Ridley, C. J.; Bull, C. L.; Wells, S. A.; Sartbaeva, A. Determining the Structure of Zeolite Frameworks at High Pressures. *CrystEngComm* **2021**, *23* (33), 5615–5623. https://doi.org/10.1039/D1CE00142F.

(27) Gigli, L.; Vezzalini, G.; Quartieri, S.; Arletti, R. Compressibility Behavior and Pressure-Induced over-Hydration of Zeolite KAlSi-L. *Microporous Mesoporous Mater.* **2019**, *276*, 160–166. https://doi.org/10.1016/J.MICROMESO.2018.09.031.

(28) Confalonieri, G.; Vezzalini, G.; Quattrini, F.; Quartieri, S.; Dejoie, C.; Arletti, R. Ce-Exchange Capacity of Zeolite L in Different Cationic Forms: A Structural Investigation. *J. Appl. Crystallogr.* **2021**, *54* (6), 1766–1774. https://doi.org/10.1107/S1600576721010827/HTTPS://JOURNALS.IUCR.ORG/SERVICES/PERMISSIONS.HTML.

(29) Vezzalini, G.; Maletti, L.; Renzo, F. Di; Arletti, R. Ion Exchange Capacity of Synthetic Zeolite L: A Promising Way for Cerium Recovery Giorgia Confalonieri European Synchrotron Radiation Facility. **2022**. https://doi.org/10.21203/rs.3.rs-1174126/v1.

(30) Treacy, M. M. J. (Michael M. J. .; Higgins, J. B.; International Zeolite Association. Structure Commission. Collection of Simulated XRD Powder Patterns for Zeolites. **2007**, 485.

(31) Scherrer, P. . Estimmung Der Grosse Und Der Inneren Struktur von Kolloidteilchen Mittels Rontgenstrahlen, Nachrichten von Der Gesellschaft Der Wissenschaften, Gottingen. *Math. Klasse* **1918**, *2*, 98–100.

(32) Mayer, F.; Zhang, W.; Brichart, T.; Tillement, O.; Bonnet, C. S.; Tóth, É.; Peters, J. A.; Djanashvili, K. Nanozeolite-LTL with GdIII Deposited in the Large and EuIII in the Small Cavities as a Magnetic Resonance Optical Imaging Probe. *Chem. – A Eur. J.* **2014**,

20 (12), 3358–3364. https://doi.org/10.1002/CHEM.201304457.

(33) Gigli, L.; Arletti, R.; Quartieri, S.; Di Renzo, F.; Vezzalini, G. The High Thermal Stability of the Synthetic Zeolite K–L: Dehydration Mechanism by in Situ SR-XRPD Experiments. *Microporous Mesoporous Mater.* **2013**, *177,* 8–16. https://doi.org/10.1016/J.MICROMESO.2013.04.015.

(34) Król, M.; Mozgawa, W.; Jastrzbski, W.; Barczyk, K. Application of IR Spectra in the Studies of Zeolites from D4R and D6R Structural Groups. *Microporous Mesoporous Mater.* **2012**, *156*, 181–188. https://doi.org/10.1016/J.MICROMESO.2012.02.040.

(35) FLANIGEN, E. M.; KHATAMI, H.; SZYMANSKI, H. A. Infrared Structural Studies of Zeolite Frameworks. **1974**, 201–229. https://doi.org/10.1021/BA-1971-0101.CH016.

(36) Ma, Y. K.; Rigolet, S.; Michelin, L.; Paillaud, J. L.; Mintova, S.; Khoerunnisa, F.; Daou, T. J.; Ng, E. P. Facile and Fast Determination of Si/Al Ratio of Zeolites Using FTIR Spectroscopy Technique. *Microporous Mesoporous Mater.* **2021**, *311*, 110683. https://doi.org/10.1016/J.MICROMESO.2020.110683.

(37) Medeiros-Costa, I. C.; Dib, E.; Nesterenko, N.; Dath, J.-P.; Gilson, J.-P.; Mintova, S. Silanol Defect Engineering and Healing in Zeolites: Opportunities to Fine-Tune Their Properties and Performances. *Chem. Soc. Rev.* **2021**. https://doi.org/10.1039/D1CS00395J.

(38) Sing, K. S. W. Reporting Physisorption Data for Gas/Solid Systems with Special Reference to the Determination of Surface Area and Porosity (Recommendations 1984). *Pure Appl. Chem.* **1985**, *57* (4), 603–619. https://doi.org/10.1351/pac198557040603.

(39) Sebastian, J.; Jasra, R. V. Sorption of Nitrogen, Oxygen, and Argon in Silver-Exchanged Zeolites. *Ind. Eng. Chem. Res.* **2005**, *44* (21), 8014–8024. https://doi.org/10.1021/IE050442P/ASSET/IMAGES/LARGE/IE050442PF00008.JPEG.

(40) Peter, S. A.; Moharir, A. S.; Jasra, R. V. Selective Adsorption of Oxygen over Argon in Alkaline-Earth-Metal Cation-Exchanged Zeolite X. *Ind. Eng. Chem. Res.* **2010**, *49* (16), 7524–7529. https://doi.org/10.1021/IE100615E/SUPPL_FILE/IE100615E_SI_001.PDF.

(41) Komaty, S.; Anfray, C.; Zaarour, M.; Awala, H.; Ruaux, V.; Valable, S.; Mintova, S. A Facile Route toward the Increase of Oxygen Content in Nanosized Zeolite by Insertion

of Cerium and Fluorinated Compounds. *Mol. 2018, Vol. 23, Page 37* **2018**, *23* (2), 37. https://doi.org/10.3390/MOLECULES23020037.

(42) Rodríguez-Galván, A.; Rivera, M.; García-López, P.; Medina, L. A.; Basiuk, V. A. Gadolinium-Containing Carbon Nanomaterials for Magnetic Resonance Imaging: Trends and Challenges. *J. Cell. Mol. Med.* **2020**, *24* (7), 3779–3794. https://doi.org/10.1111/JCMM.15065.

(43) Hermann, P.; Kotek, J.; Kubíček, V.; Lukeš, I. Gadolinium(III) Complexes as MRI Contrast Agents: Ligand Design and Properties of the Complexes. *Dalt. Trans.* **2008**, No. 23, 3027–3047. https://doi.org/10.1039/B719704G.